Selection and thermal physical characteristics analysis of in-situ condition preserved coring lunar rock simulant in extreme environment

Haichun Hao [a,b], Mingzhong Gao [a,b,*], Cunbao Li [a,b], Xuan Wang [a,b], Yan Wu [a,b], Zheng Gao [a,b], Wen Yu [c], Xuemin Zhou [a,b]

[a] Guangdong Provincial Key Laboratory of Deep Earth Sciences and Geothermal Energy Exploitation and Utilization, Institute of Deep Earth Sciences and Green Energy, College of Civil and Transportation Engineering, Shenzhen University, Shenzhen 518060, China
[b] Shenzhen Key Laboratory of Deep Underground Engineering Sciences and Green Energy, Shenzhen University, Shenzhen 518060, China
[c] Center for Lunar and Planetary Sciences, Institute of Geochemistry, Chinese Academy of Sciences, Guiyang 550081, China

A R T I C L E   I N F O

A B S T R A C T

With the increasing scarcity of Earth's resources and the development of space science and technology, the exploration, development, and utilization of deep space-specific material resources (minerals, water ice, volatile compounds, etc.) are not only important to supplement the resources and reserves on Earth but also provide a material foundation for establishing extraterrestrial research bases. To achieve large depth in-situ condition-preserved coring (ICP-Coring) in the extreme lunar environment, first, lunar rock simulant was selected (SZU-1), which has a material composition, element distribution, and physical and mechanical properties that are approximately equivalent to those of lunar mare basalt. Second, the influence of the lunar-based in-situ environment on the phase, microstructure, and thermal physical properties (specific heat capacity, thermal conductivity, thermal diffusivity, and thermal expansion coefficient) of SZU-1 was explored and compared with the measured lunar rock data. It was found that in an air atmosphere, low temperature has a more pronounced effect on the relative content of olivine than other temperatures, while in a vacuum atmosphere, the relative contents of olivine and anorthite are significantly affected only at temperatures of approximately −20 and 200 °C. When the vacuum level is less than 100 Pa, the contribution of air conduction can be almost neglected, whereas it becomes dominant above this threshold. Additionally, as the testing temperature increases, the surface of SZU-1 exhibits increased microcracking, fracture opening, and unevenness, while the specific heat capacity, thermal conductivity, and thermal expansion coefficient show nonlinear increases. Conversely, the thermal diffusivity exhibits a nonlinear decreasing trend. The relationship between thermal conductivity, thermal diffusivity, and temperature can be effectively described by an exponential function (R^2>0.98). The research results are consistent with previous studies on real lunar rocks. These research findings are expected to be applied in the development of the test and analysis systems of ICP-Coring in a lunar environment and the exploration of the mechanism of machine-rock interaction in the in-situ drilling and coring process.

1. Introduction

As the closest natural satellite to the Earth, the Moon has unique physical resources (minerals, water ice, volatiles, etc.), location resources (earth observation, asteroid defense, etc.), and environmental resources (large temperature difference, ultrahigh vacuum, etc.). The Moon has become an "outpost" for humans to step into deep space [1–5]. Previous research has shown that the abundant mineral resources of the Moon are mainly stored in lunar rocks with depths of 10 to 15 m [6,7], while the maximum depth of successfully obtained lunar samples is only 3.05 m, falling short of the lunar rock layer. In future lunar exploration missions, the sampling and return of deep lunar rock samples are inevitable. However, the thermal physical properties of deep lunar rocks are the key factors in determining the success of coring (heat dissipation, chip removal, etc.). Therefore, to effectively implement the large-depth ICP-Coring in an extreme lunar environment, the primary task is to select lunar rock simulant from Earth and test them to elucidate the thermal physical properties of lunar rock simulants under extreme conditions. This will provide a scientific basis for and engineering understanding of the exploration, development,

and utilization of lunar mineral resources, as well as the construction of extraterrestrial research bases.

In recent years, there have been many studies carried out on the drilling and coring load characteristics of lunar rock simulants. Based on the mechanical properties and drillability grade of the lunar rock simulant, researchers have selected marble, granite, sandstone, limestone, travertine and other materials as the lunar rock simulant [8–13]. In addition, some researchers [14] have studied the temperature field distribution of the interaction between coring drilling tools and lunar rock simulants using clay bricks as the lunar rock simulant. However, the lunar rock simulants selected by the above researchers did not consider the chemical composition, mineral composition and porosity, which are factors influencing the thermal physical properties [15]. As a result, these simulants failed to accurately approximate the real lunar rocks in terms of material composition and physical properties, thereby hindering a comprehensive understanding of the thermal evolution of the Moon and the thermal properties of lunar rocks. For the specific heat capacity of lunar rocks, Bastin et al. [16] found that the specific heat capacity of 10065 lunar rock is approximately (0.84 ± 0.084) J/(g·°C); Robie et al. [17] used an adiabatic calorimeter to measure the specific heat capacity of Apollo 11 lunar sample 10057 vesicular basalt between -183 and 77 °C. The specific heat capacity increased from 0.25 to 0.84 J/(g·°C) within the test range, showing an increasing trend with a decreasing rate of increase.

Regarding the thermal conductivity and thermal diffusivity of the main thermal properties of rocks, Cremers et al. [18] measured the thermal conductivity of the Apollo 11 sample (10084–68) under vacuum conditions. The test results showed that as the temperature increased from -73 to 127 °C, the thermal conductivity of the sample increased from 1.44×10^{-3} to 2.47×10^{-3} W/(m·°C). Bernett et al. [19] used broken olivine basalt to test its thermal conductivity at a temperature of -100 to 200 °C, vacuum level of 6.7×10^{-4} to 6.7×10^{-1} Pa, and standard atmospheric pressure. The results show that the measured thermal conductivity at atmospheric pressure was approximately 100 times higher than that in a vacuum. The thermal conductivity of olivine basalt increased by approximately 60% with increasing bulk density from 1.14 to 1.57 g/cm^3. It showed no significant change with the increase in vacuum level from 6.7×10^{-4} to 6.7×10^{-1} Pa, but exhibited an increasing trend with the rise in average temperature from -70 to 100 °C. At the same time, Fountain and West [20] carried out experiments on the variation in the thermal conductivity of particulate basalt with density and temperature in a simulated lunar environment, confirming that the effect of density and temperature on the thermal conductivity of particulate basalt is similar to that identified by Bernett et al. [19]. Fujii and Osako [21] tested the thermal diffusivity of three lunar rocks and two terrestrial basalts at standard atmospheric pressure and vacuum levels ranging from 10^{-3} to 10^{-1} Pa. The thermal diffusivity decreased with increasing temperature under both standard atmospheric pressure and vacuum conditions, and the disparity between the values obtained under these conditions decreased as temperature increased. The porosity of rock had a great influence on thermal diffusivity when the temperature was lower than 226.85 °C. In addition, Horai et al. [22] used the modified Angstrom method to test the thermal diffusivity of lunar samples 10057 (Type A) and 10065 (Type C) in the atmospheric environment at temperatures ranging from -130 to 150 °C. The results showed that the thermal diffusivity decreased with increasing temperature, but the test value of the breccia sample (Type C) was smaller than that of the igneous rock sample (Type A). They believed that the Type C sample had more cracks. Furthermore, Horai and Winkler [23] studied the thermal diffusivity of a medium-grained lunar porphyritic basalt sample (1200285) at standard atmospheric pressure and

10^{-3} Pa, and the test results were similar to those of Fujii and Osako [21].

Numerous studied have been carried out on the coefficient of thermal expansion of rock thermal properties. Baldridge et al. [24] studied the thermal expansion coefficients of lunar samples 10020, 10057, 12022, and 10046 at temperatures ranging from -100 to 200 °C. They found that the measured thermal expansion volume was 40% to 70% of the calculated value, and they believed that the reason for this phenomenon was that there were many cracks in the lunar rocks. Thirumalai and Demou [25] measured the thermal expansion of lunar rock simulant at atmospheric pressure and 10^{-3} Pa with a heating rate of 5 °C/min. It was found that the thermal expansion coefficient increased with increasing temperature. In addition, it was confirmed that the thermal response of the lunar rock simulant material was independent of the ambient pressure below 300 °C. Richter and Simmons [26] carried out a thermal expansion test of igneous rock at 25 to 550 °C and found that when the heating rate was not more than 2 °C/min and the temperature was lower than 250 °C, the expansion curve could be repeated, and the igneous rock had no permanent strain. When the heating rate was greater than 2 °C/min or the temperature was higher than 350 °C, the igneous rock produced new cracks and permanent strains. Griffin and Demou [27] conducted thermal expansion tests of 14 rocks at temperatures ranging from -140 to 950 °C and found that the thermal expansion of most rocks increased nonlinearly with increasing temperature. Low-density rocks showed a shrinkage trend after 550 °C, and permanent strain also appeared when the temperature was higher than 200 °C. Moreover, Cooper and Simmons [28] found that the thermal expansion coefficient of igneous rock increased faster than the average thermal expansion coefficient of its mineral composition within 25 to 400 °C.

In summary, the currently selected lunar rock simulants fail to approximate real lunar rocks in terms of material composition and physical and mechanical properties. Furthermore, there are few reports on the thermal physical properties of lunar rock simulants using mare basalt as a reference material. Therefore, this paper carefully selected lunar rock simulant that closely resemble mare basalt and investigated the influence of extreme lunar surface environments on the mineral composition and microstructure of the lunar rock simulant. Additionally, this work clarified the thermal physical properties of lunar rock simulant under extreme lunar surface conditions. This research identified appropriate lunar rock simulant samples and provided thermal physical parameters for the development and testing of ICP-Coring in a simulated lunar environment.

2. Test method and scientific verification of physical and mechanical properties of lunar rock simulant

2.1. Preparation of lunar rock simulant samples

Based on the element distribution, material composition, and basic mechanical properties of lunar mare basalt, and after extensive literature research and multiple field visits, we preliminarily selected the Chifeng basalt from Inner Mongolia, China as a lunar rock simulant (abbreviated to SZU-1 here). To meet the test requirements, we recovered approximately 2 m^3 of Chifeng basalt from a mine to ensure that the samples required for subsequent tests were all from the same rock mass to ensure the homogeneity of the test samples. According to the experimental design, this basalt was fabricated into $\Phi50$ mm $\times$ 100 mm, $\Phi20$ mm $\times$ 40 mm, $\Phi50$ mm $\times$ 25 mm, $\Phi25.4$ mm $\times$ 2 mm, and $\Phi10$ mm $\times$ 25 mm cylindrical samples to carry out experimental studies on the compressive strength, tensile strength, thermal conductivity, thermal expansion coefficient, etc. Additionally, lunar rock

simulant powder (200 mesh) was prepared, and the thermal characteristics of the lunar rock simulant in-situ environment, such as specific heat capacity, were studied via XRD and XRF. The sample preparation and pretreatment are shown in Fig. 1.

2.2. Test method for the physical and mechanical properties of lunar rock simulant

To scientifically verify the physical and mechanical properties of lunar rock simulant and real lunar rocks, first, we used Thermo Scientific ARL PERFORM'X for the total element and oxide quantitative analysis of SZU-1 in a vacuum environment. Second, the porosity of the saturated SZU-1 samples was measured by a MesoMR23-060H-I medium-sized NMR analysis and imaging system (Fig. 2). Specifically, the specimens were placed in a vacuum saturation device filled with pure water. The water level was adjusted to ensure complete submersion of the specimens. The vacuum pump was then activated to evacuate the air for a duration of 4 h, followed by 24 h of saturation. Subsequently, the specimens underwent porosity testing. Finally, the MTS 810 electrohydraulic servo-controlled material testing system (Fig. 3a) was used to test the uniaxial compressive strength and tensile strength of $\Phi 20$ mm $\times$ 40 mm and $\Phi 50$ mm $\times$ 25 mm SZU-1, which were vacuum dried for 24 h according to the rock mechanics sample preparation standard [29]. To avoid the size effect, the RMT-301 rock direct shear/triaxial compression composite testing machine (Fig. 3b) was used to test the uniaxial compressive strength of $\Phi 50$ mm $\times$ 100 mm SZU-1. The control mode used was displacement control, with a loading rate of 0.5 mm/min.

2.3. Scientific verification of lunar rock simulant

Currently, most of the lunar rock samples obtained are lunar rock particles with diameters greater than 1 cm. However, successful acquisition of samples of lunar rock layers has not yet been achieved [1]. Lunar rocks are mainly mare basalts, highland rocks, and breccia, among which mare basalts account for a large proportion [30], approximately 17% of the lunar surface area and 1% of the lunar volume [1,31]. Recently, the 1731 g lunar samples obtained by Chang'e-5 were also dominated by young basalts [32], and some researchers believe that the material composition of mare basalts can reflect the physical and chemical environment of the formation of lunar rocks, which is of great significance to the thermal evolution of the Moon and the exploration and development of lunar in-situ resources [33]. Therefore, mare basalt was taken as a reference

Fig. 2. Medium-size NMR analysis and imaging system.
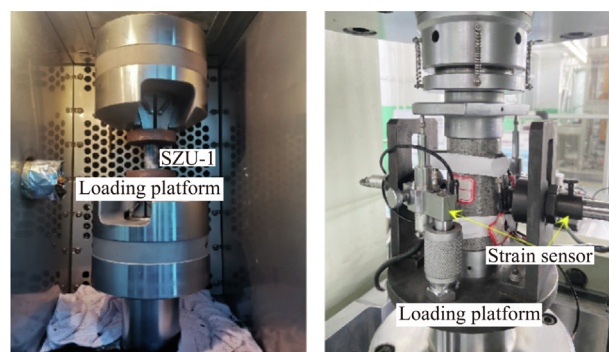
(a) MTS 810 electrohydraulic servo-controlled material testing system

(b) RMT-301 rock direct shear/triaxial compression composite testing machine

Fig. 3. SZU-1 uniaxial compressive and tensile strength test equipment.

to identify a lunar rock simulant that is close to the mare basalt in terms of mineral composition, physical properties and mechanical properties.

Research has shown that the main chemical components of mare basalt include SiO_2, TiO_2, Al_2O_3, FeO, MnO, MgO, CaO, Na_2O, K_2O, and Cr_2O_3 and that the main elements include O, Si, Al, Ca, Fe, Na, Mg, and Ti [1,34]. Through XRF testing (Fig. 4), we found that SZU-1 is consistent with the mare basalt in terms of chemical components and main element categories. In addition, we determined that the mass ratios of the main chemical components and main elements of SZU-1 listed above are 45.20%, 0.38%, 7.50%, 20.00%, 0.26%, 17.50%, 8.50%, 0.13%, 0.03%, 0.53% and 45.89%, 24.89%, 10.34%, 6.66%, 5.55%, 2.74%, 2.39%, 0.70%, respectively. Through comparative analysis with the existing real lunar rock test data (Fig. 4), the chemical composition and the content of main elements of SZU-1 are between the extreme values of the existing test data. For chemical composition, French et al. [6] concluded that lunar basalt and terrestrial basalt have similar SiO_2 contents, both of which are less than 54%, and the measured SiO_2 contents of SZU-1 also verify this conclusion. Meanwhile, taking TiO_2 content (weight percent, %) as one of the most significant characteristics to identify basalt, basalt is divided into high-Ti (>9%), low-Ti (1.5%–9%), and very low-Ti (<1.5%) categories, and the SZU-1 TiO_2 content is 0.38%, belonging to very low-Ti basalt. Notably, the occurrence form of Fe is 3^+ in terrestrial basalt but 2^+ in lunar basalt [6]. The measured results show that the occurrence form of Fe in SZU-1 also conforms to this trend; that is, the occurrence form of iron oxide in SZU-1 in Fig. 6 is Fe_2O_3. Among
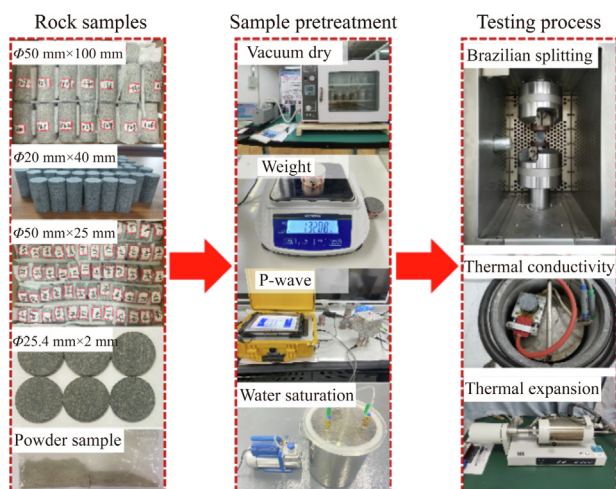

Fig. 1. SZU-1 preparation and pretreatment.

(a) Chemical composition of lunar rocks and SZU-1

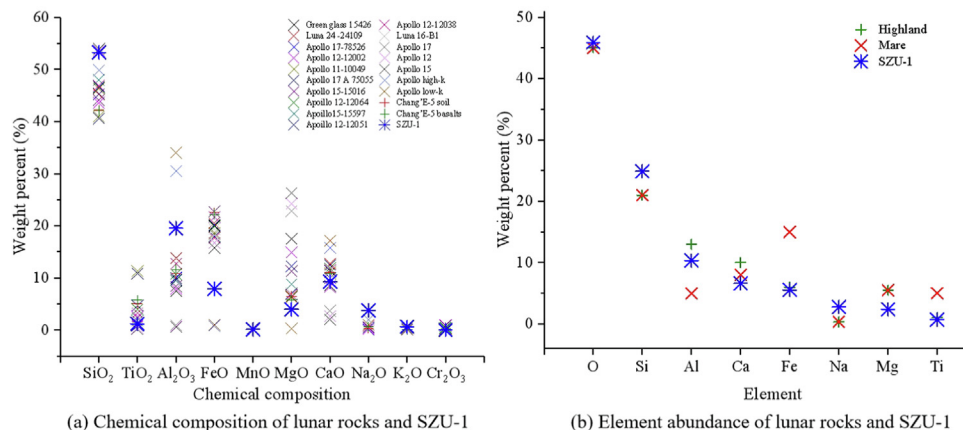(b) Element abundance of lunar rocks and SZU-1

Fig. 4. Chemical composition and element abundance of lunar rocks and SZU-1 [1,6,35].

the main elements listed above, the minimum differences between SZU-1 and real lunar rocks are 0.89%, 3.89%, 2.66%, 1.34%, 0.45%, 2.38%, 3.11% and 0.3%, respectively. Therefore, SZU-1 can be approximately used to simulate lunar mare basalt in terms of chemical and element composition.

We further verified and analyzed the basic physical and mechanical characteristics of SZU-1. As shown in Table 1 and Fig. 5, the average natural density of SZU-1 is approximately 2.737 g/cm³, the porosity does not exceed 1.7958%, and most of the pores are transition pores (0.01 μm≤r<1 μm). The rock itself is relatively compact, without obvious cracks. The P-wave velocity (Table 1) also reflects this phenomenon laterally. In addition, Fig. 6 shows that the average uniaxial compressive strength of SZU-1 considering the size effect is 178.61 to 240.59 MPa and that the average tensile strength is 11.76 MPa. According to existing studies, the porosity of mare basalt is 0 to 10%, the uniaxial compressive strength is approximately 200 MPa, and the dynamic tensile strength is approximately 114 to 160 MPa [36,37]. According to the conversion relationship between dynamic and static tensile strengths measured by Cohn and Ahrens [38], it can be calculated that the static tensile strength of lunar basalts is approximately 6.1 to 24.18 MPa, and our measured results show that the basic physical and mechanical properties of SZU-1 and lunar basalts are similar. Therefore, in terms of basic physical and mechanical properties, SZU-1 can be approximately used as to simulate lunar mare basalt.

3. Phase and microstructure of SZU-1 in-situ lunar-based environment

3.1. Phase characteristics of SZU-1 in-situ lunar-based environment

By studying mare basalts, researchers have formed a relatively unified understanding that the main minerals in the mare basalt are augite, plagioclase, and olivine, among which plagioclase is dominated by anorthite [1,39]. Therefore, we used Smart Lab (Co-Kα radiation generated at 40 kV and 200 mA), an intelligent X-ray polycrystal diffractometer, to study the phase characteristics
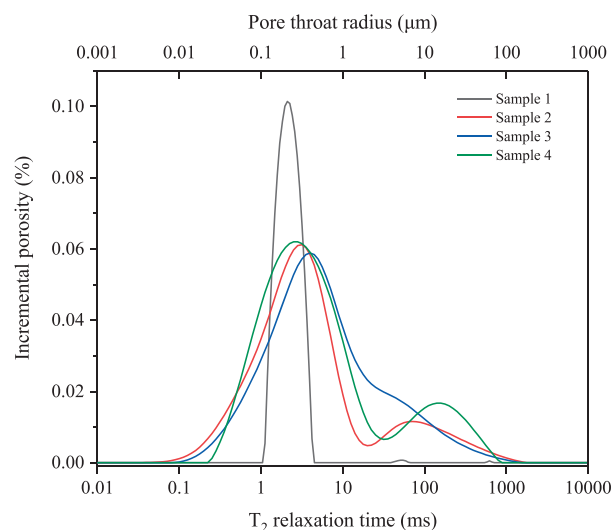

Fig. 5. SZU-1 pore distribution.

of SZU-1 powder samples (200 mesh) at extreme lunar temperatures in air and vacuum atmospheres in real time. The scanning speed was 0.02 (°)/s, the scanning range was 10° to 80°, and the temperature holding time was 5 min. Based on the above test results, the Rietveld method was used to quantitatively refine the three main minerals by Jade software. The refinement index was expressed as a weighted factor R (Eq. (1)) and an expected value E (Eq. (2)) (EPS=0.5) [40].

$$R = 100 \cdot \sqrt{\frac{\sum w(i) \cdot [I(o,i) - I(c,i)]^2}{\sum w(i) \cdot [I(o,i) - I(b,i)]^2}} \tag{1}$$

$$E = 100 \cdot \sqrt{\frac{N - P}{\sum I(o,i)}} \tag{2}$$

Table 1
SZU-1 basic physical parameters and porosity.

Sample number	Natural density (g/cm³)	Dry density (g/cm³)	Dry longitudinal wave velocity (m/s)	Porosity (%)
1	2.744	2.722	5494.51	1.3142
2	2.758	2.739	5530.39	1.5326
3	2.717	2.704	5347.59	1.6944
4	2.729	2.711	5376.34	1.7958

(a) USC of $\Phi50$ mm×100 mm

(b) USC of $\Phi20$ mm×40 mm
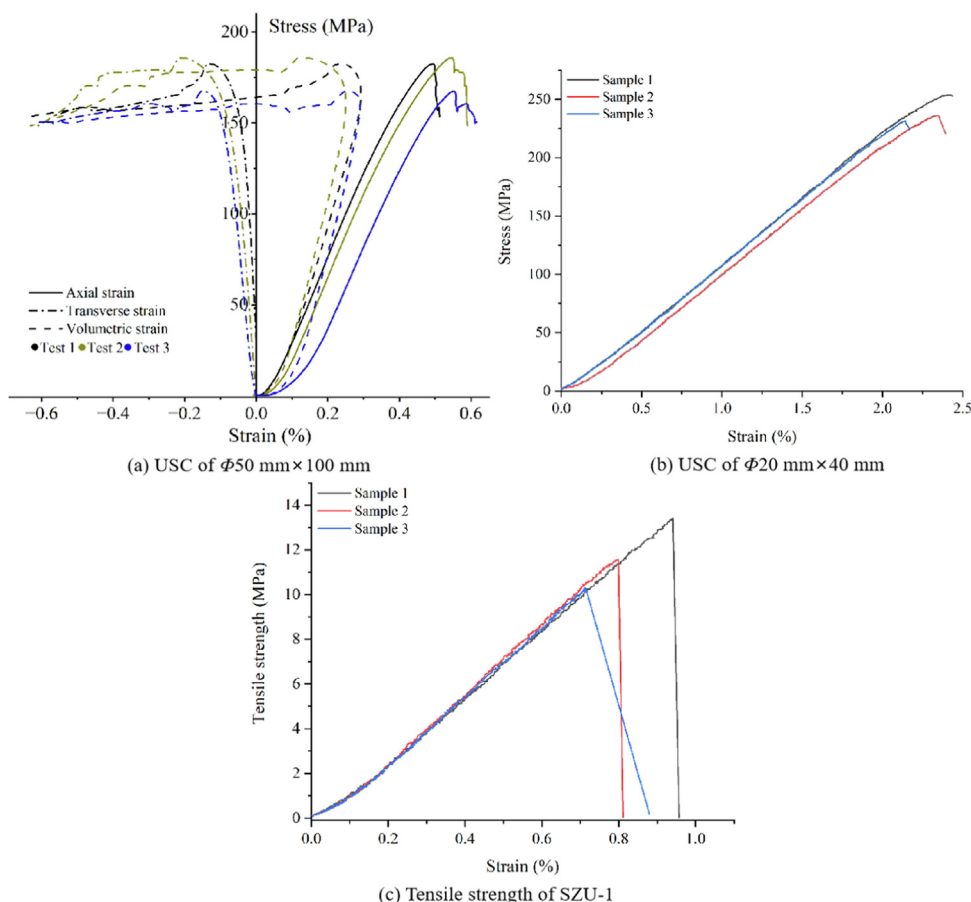
(c) Tensile strength of SZU-1

Fig. 6. SZU-1 basic mechanical characteristic curve.

where $I(o, i)$ is the measurement intensity of fitting data point i; $I(c, i)$ the calculated strength of this point; $I(b, i)$ the background strength of this point; $w(i)$ the counting weight of the point; N the number of fitted data points; and P the number of refinishing able parameters.

Through refinement, the weight factor R gradually decreases and approaches the expected value E. The Rietveld refinement map and quantitative analysis results of in-situ temperature XRD of augite, anorthite and olivine in air and vacuum atmospheres are shown in Figs. 7 and 8.

Based on Figs. 7 and 8, it can be observed that the maximum weighted factor R values for the refined air and vacuum atmosphere using the XRD-Rietveld method are 8.98% and 11.02%, respectively. The minimum values are 8.70% and 8.95%, and the average values are 8.88% and 10.11%. The refined R values are all below 15%, indicating the reliability of the quantitative analysis results [40]. Since the Rietveld method is a full-profile fitting technique, the total content of the three minerals analyzed is 100%, representing the mass distribution percentage of each mineral. From Fig. 7d, it can be observed that in the air atmosphere, the relative content of anorthite remains relatively stable. With decreasing temperature, the relative content of olivine shows a significant increasing trend, except between −20 and −50 °C, and between 30 and 50 °C, where it exhibits a decreasing trend. The maximum and minimum values of olivine content at these temperatures are 2.24 and 0.31 times that of the olivine content at room temperature, respectively. Conversely, the relative content of augite shows an increasing trend. From Fig. 8d, it can be observed that in the vacuum atmosphere, the relative content of the three minerals exhibits nonuniform variations with temperature. Anorthite and

olivine show significant changes in relative content, with opposite trends. Between −170 and −50 °C, the relative content of the three minerals changes slightly. At approximately −20, 30 to 100 °C, and 100 to 200 °C, the olivine content shows significant increasing, decreasing, and rapidly increasing trends, respectively. The observed maximum and minimum values of olivine content are 1.86 and 0.63 times that of the olivine content at room temperature, respectively. This indicates that the mineral content is influenced by the surrounding environment.

Based on the above test results, we believe that the variations in the relative content of minerals within the tested temperature range may be attributed to phase transition, crystallization, and transformation of nonequilibrium minerals (such as carbonates, hydrogen-bonded oxides, and basaltic glass) [41,42]. Fig. 11 shows that within the temperature range of −30 to 120 °C, the specific heat capacity fluctuates, suggesting the presence of unstable crystalline changes in SZU-1, resulting in fluctuations in absorbed or released heat. This supports the observed trends in the relative content of minerals. Furthermore, considering the Mohs hardness of augite, anorthite, and olivine, which are 5.5–6, 6–6.5, and 6.5–7, respectively, the variations in their relative contents with atmospheric conditions and temperature may serve as a microscopic explanation for the macroscopic changes in rock mechanics properties.

3.2. Morphological characterization of lunar rock simulant in the extreme lunar environment

In recent years, an increasing number of researchers have applied FIB microscopy technology to Earth and planetary science
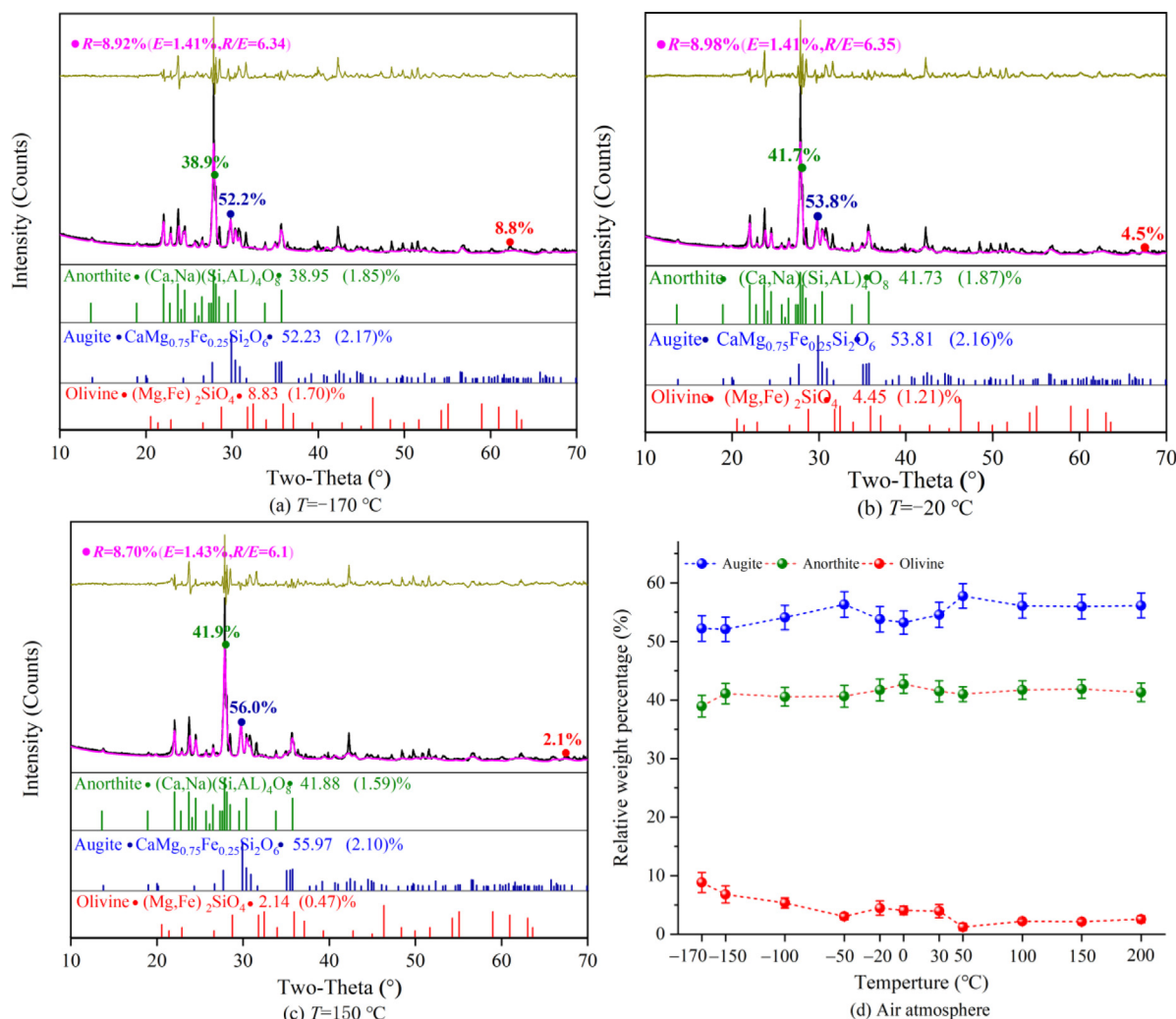
Fig. 7. In-situ temperature XRD-Rietveld refinement map and quantitative analysis results of augite, anorthite and olivine in the lunar rock simulant under air atmosphere.

research, aiming to explore the influence of extreme environments on the microstructure of samples and interpret the resulting macroscopic phenomena [43]. Given this, we used the FIB-SEM FEI Scios 2 DualBeam System (Fig. 9) to observe the 3D morphology of the dry SZU-1 surface at magnifications of 1000, 5000, and 10000 pixels under the real-time action of extreme lunar temperatures. First, we separated the surfaces of the SZU-1 samples that underwent real-time high- and low-temperature effects, firmly adhered each to the sample table with carbon conductive tape and used an SBC-12 ion sputtering instrument to gold plate the surface of the sample to form a conductive film. Second, the sample stage was fixed on the equipment-bearing platform, and the test chamber was vacuumed. Furthermore, the electron beam voltage of the device was set to 10 kV, and the current was adjusted to 0.4 nA. Finally, the corresponding sample surface was viewed through the console, and the 3D morphology was observed. The specific equipment and operation are shown in Fig. 9, and the observation results are shown in Fig. 10.

Fig. 10a shows that the surfaces of SZU-1 are more compact and smoother at low temperatures (-120 to $0\ °C$) than at room temperature ($30\ °C$). At high temperatures ($60–200\ °C$), the surfaces appear wavy and rough, accompanied by many microcracks and fissures. By further adjusting the magnification to 5000 pixels (Fig. 10b), the thermal damage defects on the surface of SZU-1 at high temperatures are more obvious than those at room tempera-

ture and low temperatures. Specifically, there are obvious cracks between mineral particles that have a certain opening. When the magnification is adjusted to 10000 pixels (Fig. 10c), the surface of a high-temperature sample is extremely uneven, and penetrating cracks between minerals are visible. Notably, at low temperatures, the SZU-1 surface has small bubble-shaped particles that nearly cover the entire observation area, making the sample surface more uniform and flatter. To summarize the experimental phenomena, we believe that under the action of high temperature, the thermal conductivity and thermal expansion coefficient of each mineral (augite, feldspar, olivine, etc.) of SZU-1 are different [44–46], leading to uneven mineral expansion during heating and thus an increase in microcracks and crack openings between minerals with increasing temperature; the resulting increases in sample surface roughness and unevenness may weaken the overall strength of the rock. The main factor affecting the surface morphology of the dry SZU-1 test samples at low temperatures is that the mineral particles shrink when cooled, resulting in closer contact between the particles and densification (the surface of a sample becomes flatter), which may strengthen the overall strength of the rock. Compared with the relatively uniform small bubble-shaped particles formed on the surface of the rock under the action of low temperature, it is possible that the liquid nitrogen directly acts on the rock, resulting in the formation of small ice crystals on the surface. However, it is more likely that the fine-grained
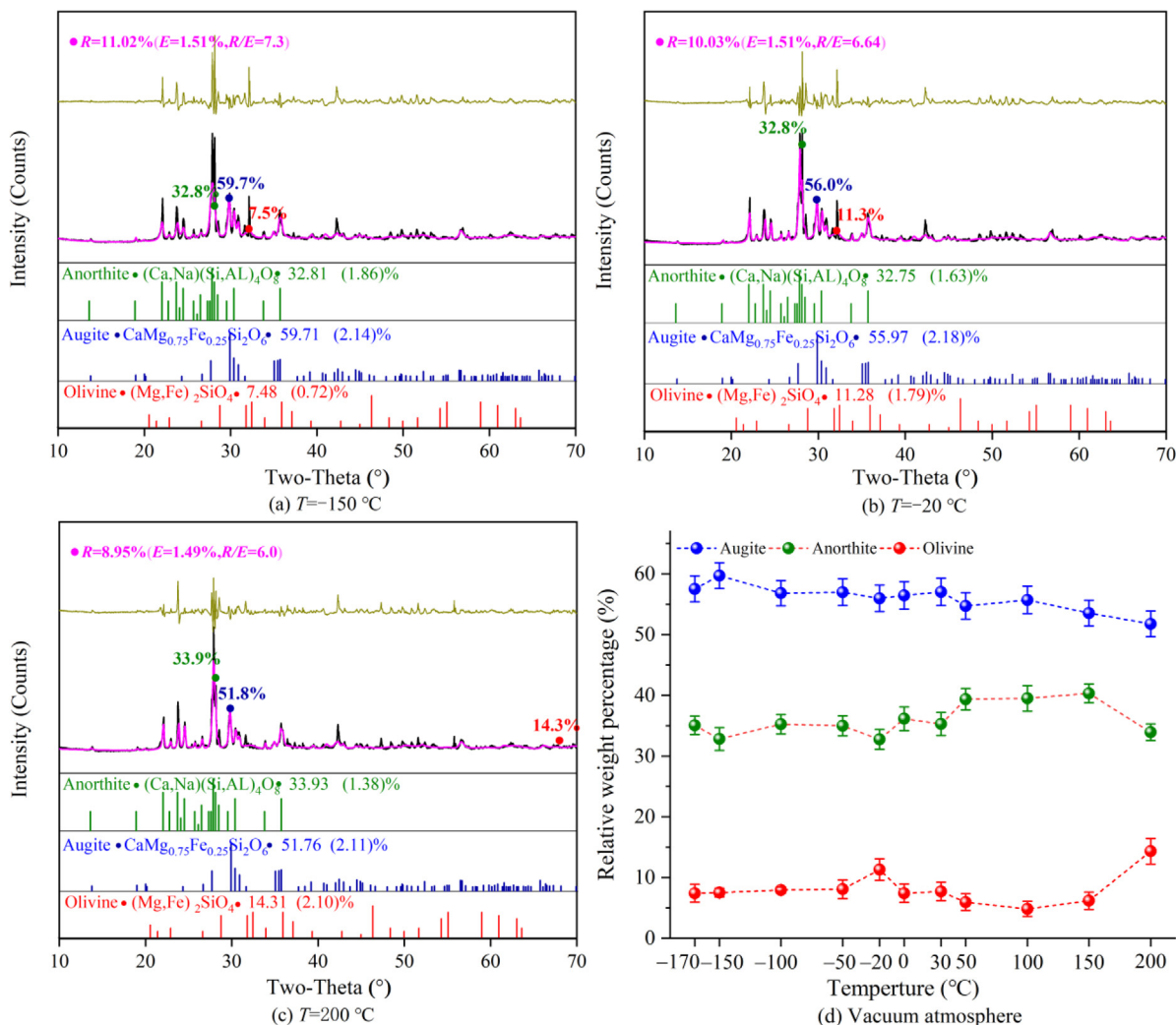
Fig. 8. In-situ temperature XRD-Rietveld refinement map and quantitative analysis results of augite, anorthite and olivine in the lunar rock simulant under vacuum atmosphere.
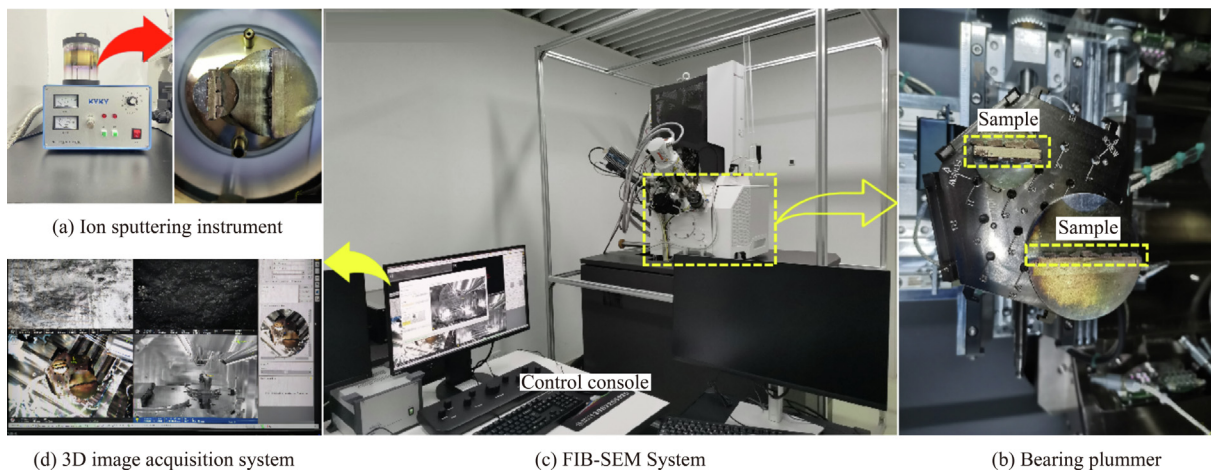

Fig. 9. FIB-SEM system and operation process.

structural minerals in SZU-1 are cooled, leading to the formation of smaller and equally sized crystalline grains, as similar phenomena have been observed in other rocks during the cooling process [47].

In summary, the lunar-based extreme environment has a certain impact on the phase and micromorphology of SZU-1, which is likely to affect the rock strength characteristics. This information
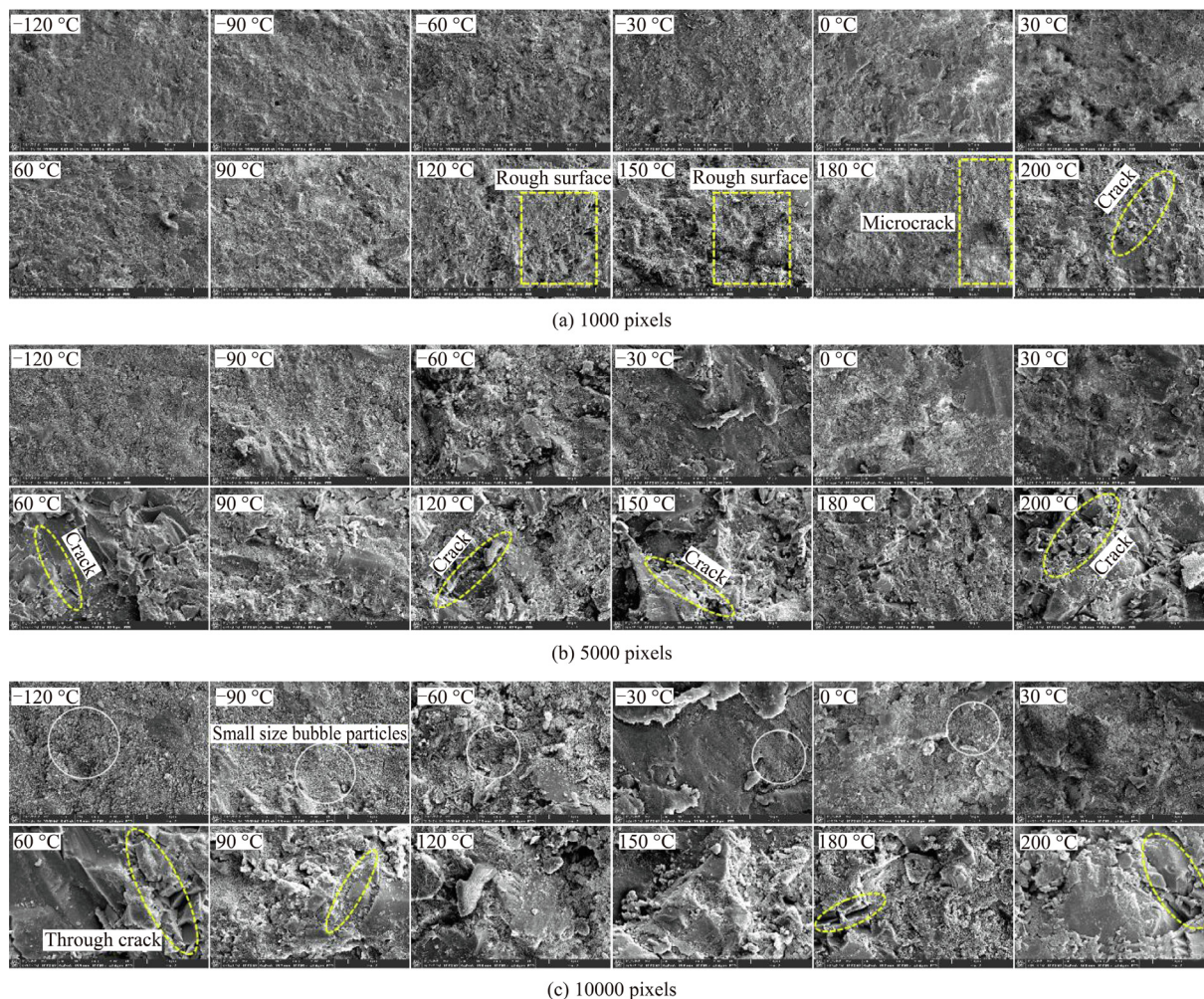
(a) 1000 pixels

(b) 5000 pixels

(c) 10000 pixels

Fig. 10. 3D surface morphology observation of SZU-1 under real-time action of lunar-based extreme temperature.

can be used to interpret the microscale characteristics of rock strength to predict its behavior at the macroscale and as data for the selection of sampling drilling tools and the design of rock-breaking techniques for lunar-based coring robots.

4. Thermal physical characteristics of lunar rock simulant in the extreme lunar environment

The specific heat capacity, thermal conductivity, and thermal expansion coefficient are vital thermal parameters of lunar rock simulants [21,24]. They not only reflect heat exchange in the extreme lunar environment, but also provide a scientific basis for the selection and design of drilling tool materials for lunar-based coring robots and drilling procedures to prevent overheating and drill stoppage.

4.1. Specific heat capacity test for lunar-based extreme environments

To elucidate the trend of the variation in the specific heat capacity of SZU-1 in the extreme lunar environment, we tested the specific heat capacity curve of SZU-1 powder (200 mesh) with varying temperature by using the sapphire method through DSC 200 F3. In this experiment, liquid nitrogen was used as a refrigeration medium, the heating/cooling rate was 10 °C/min, and the temperature test range was −150 to 250 °C. The specific calculation principle is shown in Eq. (3):

$$C_{\mathrm{p}}^{\mathrm{smp}} = C_{\mathrm{p}}^{\mathrm{std}} \cdot \frac{m_{\mathrm{std}}}{m_{\mathrm{smp}}} \cdot \frac{\mathrm{DSC}_{\mathrm{smp}} - \mathrm{DSC}_{\mathrm{bas}}}{\mathrm{DSC}_{\mathrm{std}} - \mathrm{DSC}_{\mathrm{bas}}} \tag{3}$$

where $C_{\mathrm{p}}^{\mathrm{smp}}$ and $C_{\mathrm{p}}^{\mathrm{std}}$ are the specific heat capacities of the sample to be tested and sapphire respectively, J/(mg·°C); m_{smp} and m_{std} the masses of the sample to be tested and sapphire respectively, mg; and $\mathrm{DSC}_{\mathrm{smp}}$, $\mathrm{DSC}_{\mathrm{std}}$, and $\mathrm{DSC}_{\mathrm{bas}}$ the DSC values of the sample, sapphire, and baseline respectively under the test temperature.

Considering that the equipment limit temperature is −150 °C, to prevent the test data from drifting under the influence of the environment, we used the test data at −120 to 250 °C, as shown in Fig. 11.

Fig. 11 shows that the specific heat capacity of SZU-1 increases rapidly when the test temperature range is approximately −120 to −30 °C. The specific heat capacity increases from 0.41295, 0.36228, and 0.45116 J/(g·°C) at −120 °C to 0.66923, 0.55590, and 0.87926 J/(g·°C) at −30 °C, with an average increase of 0.29267 J/(g·°C). In the range of −30 to 110 °C, the specific heat capacity of SZU-1 fluctuates. We believe that at this temperature range, crystal precipitation of unstable minerals may occur, leading to an uneven change in heat absorbed/released during the heating process, which is called the transition stage. When the test temperature range is approximately 110 to 250 °C, the specific heat capacity of SZU-1 shows a stable increasing trend. Specifically, at 110 °C, the specific heat capacity of SZU-1 is 0.92031, 0.79683, and 1.203 45 J/(g·°C), increasing to 1.04627, 0.877, and 1.35716 J/(g·°C) at

250 °C. The average increment was 0.11995 J/(g·°C). Overall, as the temperature increased, SZU-1 demonstrated a nonlinear increase in specific heat capacity, with an average increment of 0.68468 J/(g·°C). The result shows the same trend as the test results obtained by Robie et al. [17] for the Apollo 11 sample 10057 vesicular basalt. In addition, by comparing the specific heat capacity of 10065 lunar rock at normal temperature (25 °C) of (0.84±0.084) J/(g·°C) with the mean specific heat capacity of SZU-1 of 0.88778 J/(g·°C) [16], the minimum error between the two is only 0.426%. These results show that the lunar rock simulant and lunar basalts have similar specific heat capacity characteristics.

4.2. Thermal conductivity and thermal diffusivity of lunar-based extreme environment

To investigate the influence of lunar-based extreme environments on the thermal conductivity of lunar rock simulants, this study employed a low-temperature and low-pressure thermal conductivity testing system (Fig. 12) [48]. Based on the transient plane source method, the thermal conductivity of Φ50 mm $\times$ 25 mm SZU-1 samples was measured under varying vacuum (1 Pa to 1 atm) and temperature (−40 to 30 °C) conditions. The test results are shown in Fig. 13a and b. In addition, to determine the influence of temperature on the thermal diffusivity and thermal conductivity of SZU-1, we used the LFA 467 laser-flash apparatus to measure the thermal diffusivity of Φ25.4 mm $\times$ 2 mm SZU-1 samples. The temperature range of the equipment is −100 to 500 °C, and the measurement range of the thermal diffusivity is 0.01 to 1000 mm^2/s. The test equipment and schematic diagram are shown in Fig. 14, and the specific results are shown in Fig. 15. At the same time, the thermal conductivity of SZU-1 at different temperatures is calculated by Eq. (4) based on the specific heat capacity and thermal diffusivity of the measured temperature:

$$\lambda(T) = k(T) \cdot C_P(T) \cdot \rho(T) \tag{4}$$

where λ is the thermal conductivity, W/(m·°C); k the thermal diffusivity, mm^2/s; C_P the specific heat capacity, J/(g·°C); ρ the density, g/cm^3; and T the temperature, °C.

Considering that the temperature range was −90 to 200 °C and all samples tested were taken from the same rock mass, the density was taken as the dry density of 2.700 g/cm^3. The specific parameter
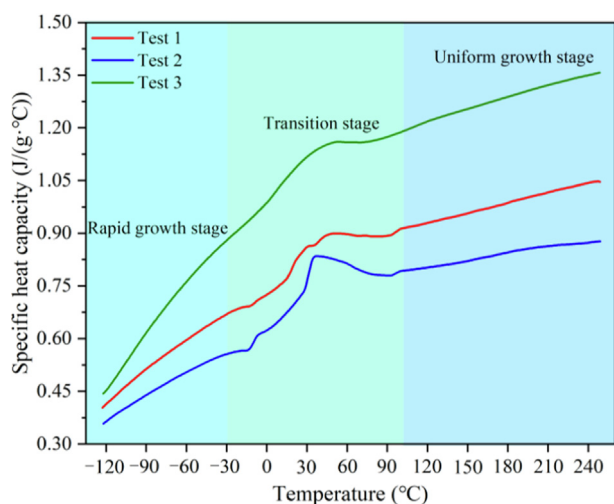
values are shown in Table 2, and the calculation results are shown in Fig. 13c.

During the experimental process, when the temperature was −40 °C and the vacuum level was 1 atm, the refrigeration system of the vacuum freeze dryer experienced severe frosting due to the combined effects of temperature and pressure. As a result, the actual temperature did not reach the desired −40 °C test temperature, and no valid data could be obtained. Fig. 13a and b shows that the thermal conductivity of SZU-1 at different temperatures has a consistent variation trend with the vacuum level, an increasing trend, which is consistent with the changing trend of the measured thermal conductivity of the main lunar mineral pyroxene observed by Yu et al. [48]. In addition, when the vacuum level is reduced from 1 atm (10000 Pa at −40 °C) to 1 Pa, the mean thermal conductivity of −40 to 30 °C decreases by 97.52%, 96.67%, 94.34%, 97.06%, 97.36%, 96.34%, 92.91%, and 94.27%, respectively. In the test range, the vacuum levels of 100 to 500 Pa have the greatest influence on thermal conductivity. At −40 to 30 °C, the average thermal conductivity at 500 Pa is approximately 10.63, 10.72, 7.43, 10.32, 10.44, 8.54, 6.58, and 7.18 times that at 100 Pa. When the vacuum level is less than 100 Pa, the thermal conductivity tends to be gentle with the decrease of the vacuum level. It has been shown that when the vacuum level is less than 1 Pa, the temperature has almost no influence on the thermal conductivity [49], which is the same trend found in this test. When the vacuum level is greater than 500 Pa, the thermal conductivity does not change significantly with increasing vacuum level. Compared with solid conduction, air conduction, and radiation conduction [48], we speculated that when the vacuum level is less than 100 Pa, air conduction can be almost ignored. However, when the vacuum level is greater than 500 Pa, air conduction is the main form of heat transfer.

When the test temperature is 30 and 60 °C, the specific heat capacity of the sample is in an unstable state, which leads to the drift of the calculated data. Therefore, quantitative analysis is not carried out in this study. It can be seen from Fig. 13c that the thermal conductivity of SZU-1 shows a nonlinear increasing trend with increasing temperature, which is consistent with the test results of Cremers et al. [18] and Bernett et al. [19] on real lunar basalt. At the same time, the thermal conductivity increases by 0.048, 0.114, 0.108, 0.152, 0.012, 0.007, 0.015, and 0.004 W/(m·°C) for the corresponding temperature increase gradients within the test range, indicating that the increase in thermal conductivity decreases with increasing temperature. Comparing the calculated and measured thermal conductivity results at temperatures of −30 and 0 °C, the corresponding temperature point errors are 4.729% and 5.852%, which shows that the reliability of the calculated result is high. In addition, we fit the relationship between thermal conductivity and temperature to obtain Eq. (5):

$$\lambda = 1.744 + 0.138 \cdot \left[1 - \exp\left(-\frac{T}{127.968}\right)\right] + 0.138$$
$$\cdot \left[1 - \exp\left(-\frac{T}{127.983}\right)\right] \tag{5}$$

The correlation coefficient is R^2=0.9842, which indicates that an exponential function can effectively characterize the relationship between thermal conductivity and temperature.

As seen from the data from the test temperature range (Fig. 15a–c), the thermal diffusivity of SZU-1 shows a nonlinear decreasing trend as the temperature increases. By calculating the mean value of the test data of three samples (Fig. 15d), considering the corresponding increasing gradient within the test temperature range, the experimental value of thermal diffusivity decreases by 0.138, 0.047, 0.034, 0.033, 0.034, 0.025, 0.021, 0.017, 0.015, and
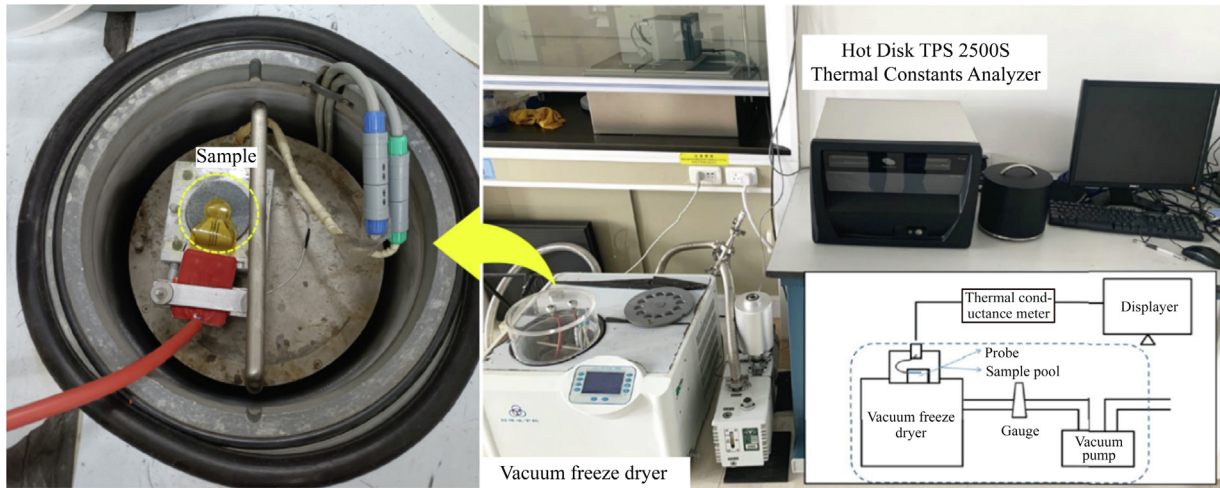

Fig. 11. Specific heat capacity of SZU-1 under lunar-based extreme temperature.

Fig. 12. Low-temperature and low-pressure thermal conductivity test system [48].
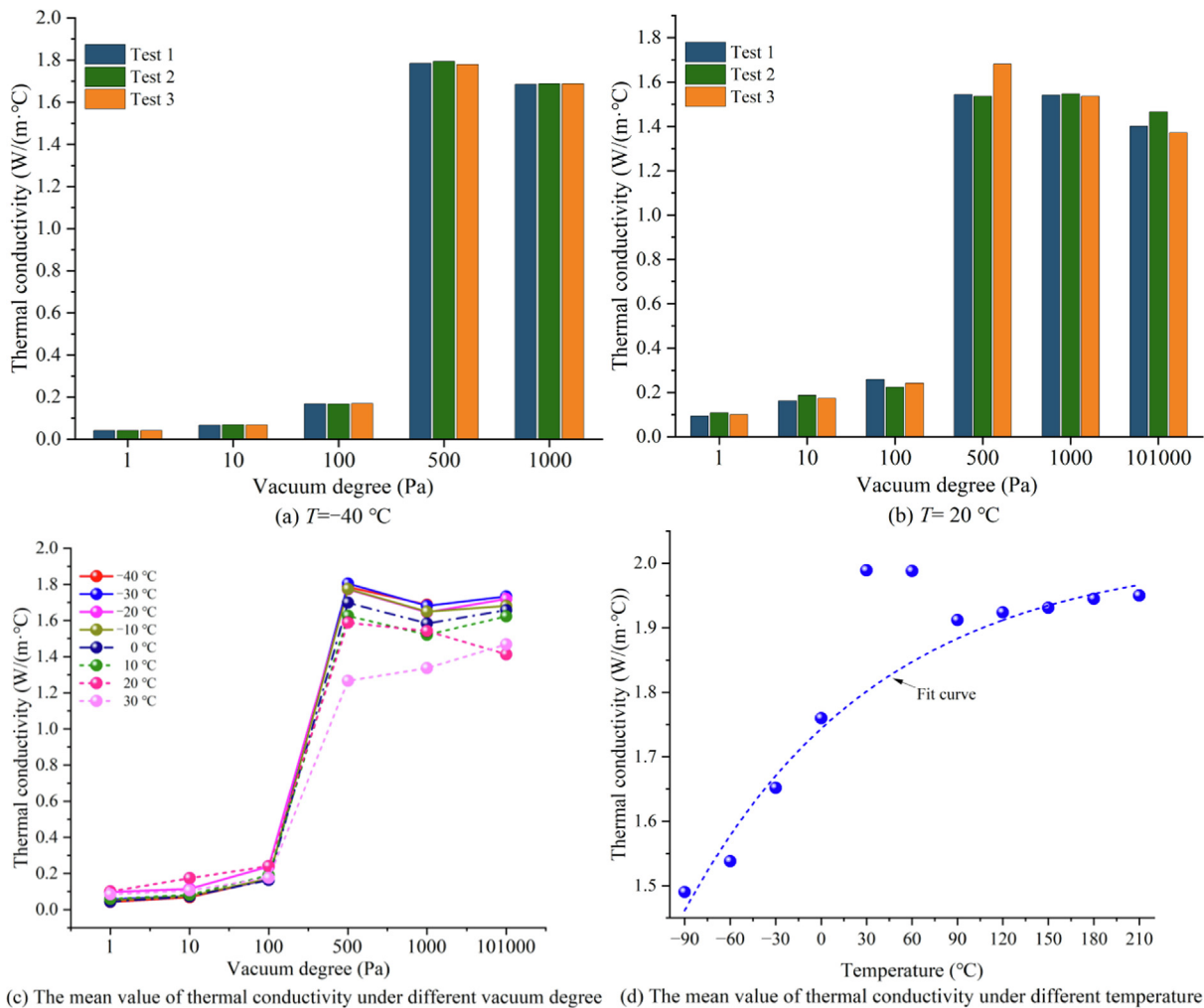

Fig. 13. Thermal conductivity curve with vacuum degree.

0.017 mm^2/s, respectively, and the decreasing amplitude became gentler. This trend is similar to the test results of lunar and terrestrial basalts by Fujii and Osako [21] and Horai et al. [22,23]. Through this test, we found that at low temperatures, the discreteness of the test data under the influence of temperature tends to increase compared with that at high temperatures. The mean test thermal diffusivity results of SZU-1 at −60, 30, 120, and 210 °C are compared with the mean thermal diffusivity results of lunar rock and terrestrial basalt by Fujii and Osako at −73, 27, 127, and 227 °C [21], the error is approximately 13.46%, 20.32%,
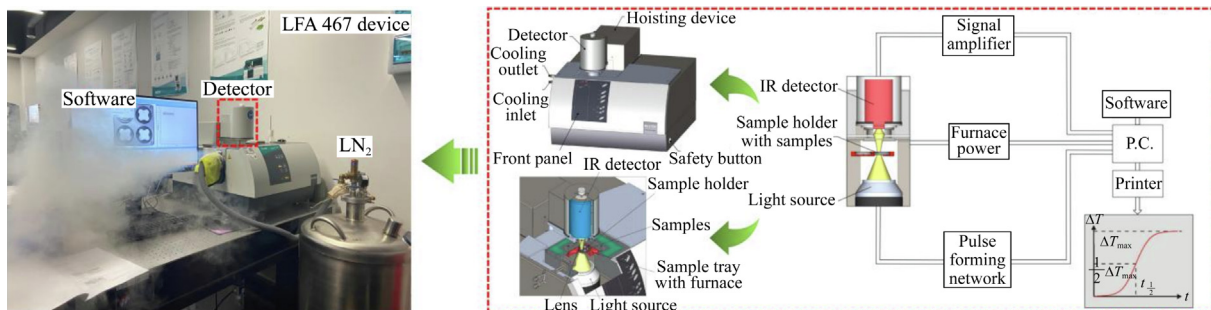
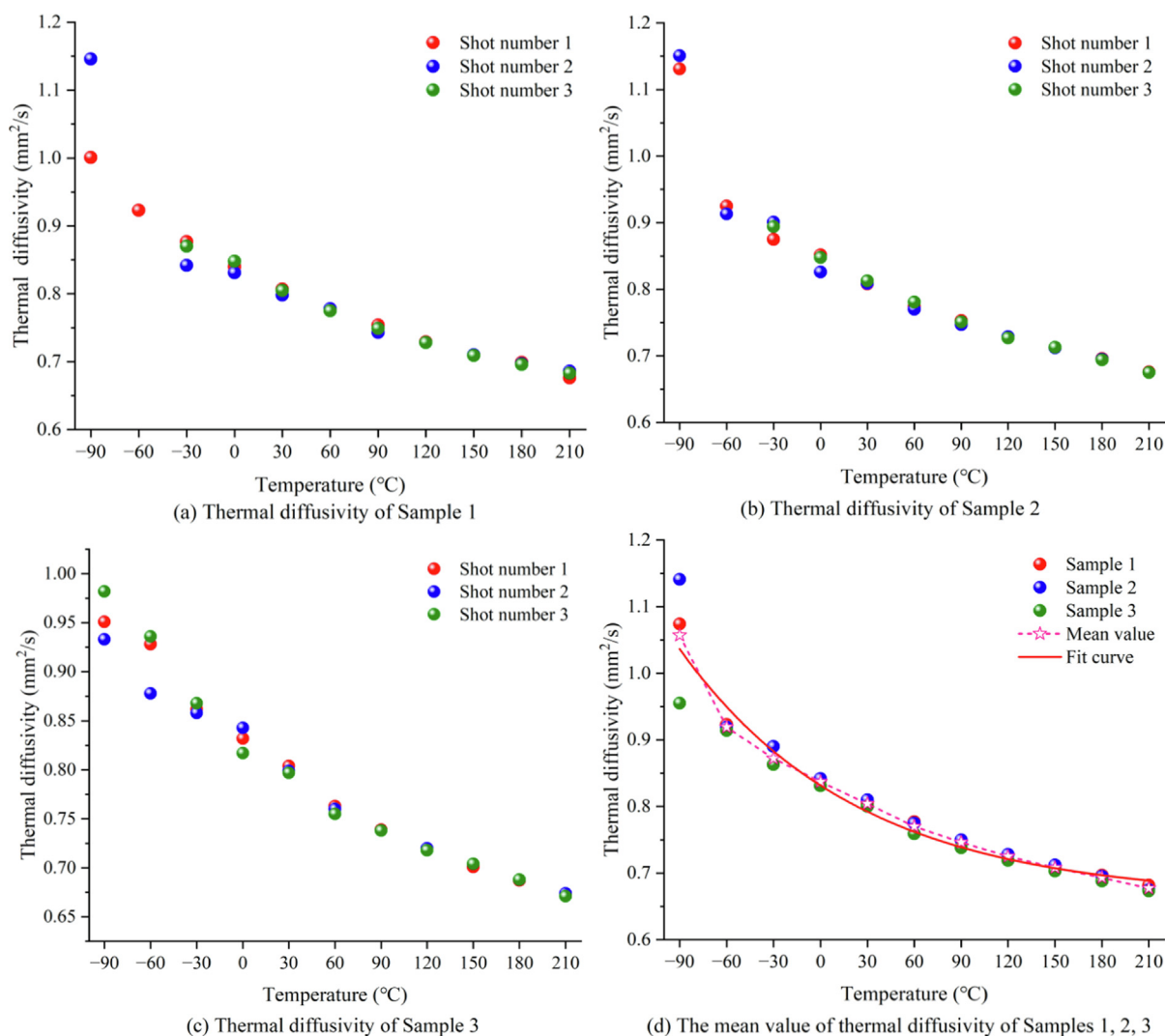**Fig. 14.** LFA 467 device and the schematic diagram.

Fig. 15. Thermal diffusivity curve of SZU-1 with temperature.

23.68%, and 28.02% for lunar rock and 22.45%, 11.45%, 5.60%, and 0.59% for terrestrial basalt, of which the minimum error is only 0.59%, and the SZU-1 test value is distributed between the test values of the other rocks [21]. Furthermore, by fitting the relationship between thermal diffusivity and temperature, we can obtain Eq. (6):

$$k = 0.170 \times \exp\left(-\frac{T}{113.541}\right) + 0.662 \tag{6}$$

The correlation coefficient is $R^2=0.9853$, which indicates that an exponential function can effectively characterize the relationship between thermal diffusivity and temperature.

4.3. Thermal expansion of lunar-based in extreme environment

To clarify the influence of lunar-based extreme environments on the thermal expansion characteristics of SZU-1, the DIL420C thermal expansion analyzer was used to conduct coefficient of

Table 2
Values of thermal parameters at different temperatures.

Temperature (°C)	Thermal diffusivity (mm²/s)	Specific heat capacity J/(g·°C)	Dry density (g/cm³)
−90	1.057	0.522	2.700
−60	0.919	0.620	2.700
−30	0.872	0.701	2.700
0	0.837	0.779	2.700
30	0.804	0.916	2.700
60	0.770	0.956	2.700
90	0.746	0.949	2.700
120	0.725	0.983	2.700
150	0.708	1.010	2.700
180	0.693	1.040	2.700
210	0.677	1.067	2.700

expansion tests on Φ10 mm × 25 mm SZU-1 samples at heating rates of 5 and 2 °C/min. The equipment temperature test range was −180 to 2000 °C, and the refrigeration medium was liquid nitrogen. The DIL420C device and schematic diagram are shown in Fig. 16. Considering the data drift of the equipment at extreme low temperatures, we used the −150 to 200 °C data for analysis. The specific test data results are shown in Fig. 17.

It can be seen from Fig. 17 that whether the temperature change rate is 2 or 5 °C/min, the corresponding test data have a very high similarity, and the thermal expansion coefficient of SZU-1 increases nonlinearly with increasing temperature on the whole. This trend is similar to the actual lunar rock test results of Thirumalai and Demou [25] and Griffin and Demou [27]. When the heating rate is 5 °C/min, the tested sample shrinks, with slight changes at approximately 10, 60, and 180 °C. We think that the cause of the above phenomenon may be the excessive heating rate, resulting in uneven heat transfer in the internal temperature field of the sample. When the heating rate is 2 °C/min, the test curve is smoother than that of 5 °C/min, thus effectively verifying the reliability of the heating rate of no more than 2 °C/min recommended by Richter and Simmons [26]. Since the two heating rate test values intersect, we believe that the heating rate has little effect on the thermal expansion characteristics of SZU-1 when the temperature is within the range of 35 to 50 °C. In addition, the SZU-1 test results are generally higher than the corresponding results of the Apollo 10046, 14318, 15418, 15015, and 10057 lunar rock samples. This conclusion is similar to the result that the Fairfax database tested by Baldridge et al. [24] is higher than the Apollo lunar rock samples.

In conclusion, the factors affecting the thermal physical properties of lunar rock simulant can be divided into intrinsic factors related to mineral composition and extrinsic factors associated with extreme lunar environments. Specifically, such intrinsic fac-

tors include the crystallization of unstable mineral components due to heating, uneven thermal stresses caused by anisotropic mineral particles, and the thermal contact state between mineral particles [23–25,28]. Extrinsic factors related to extreme lunar environments include extreme temperature conditions and different heat conduction modes under varying vacuum levels [48,50]. The influence of simulated extreme lunar environments on the specific heat capacity, thermal diffusivity, thermal conductivity, and thermal expansion coefficient of SZU-1 lunar rock simulant is similar to the measured results of real lunar rocks. This further indicates that the chosen lunar rock simulant can be considered Earth analogs for real lunar rocks, enabling subsequent experiments and providing scientific data for the design of lunar-based ICP-Coring robots.

5. Conclusions

To explore the principle and technology of large-depth ICP-Coring in an extreme lunar environment, we selected lunar rock simulants that are approximately equivalent to real lunar rocks in terms of physical and mechanical properties and analyzed their in-situ environmental phases and micromorphological characteristics. In addition, the influence of extreme environments on their thermal properties was preliminarily explored.

(1) In the air atmosphere, the low temperature has a significant effect on the relative content of olivine. In the vacuum atmosphere, the relative contents of olivine and anorthite were greatly affected when the temperature is approximately −20 and 200 °C. Moreover, with the increase in temperature, the surface microcracking, crack opening, and unevenness of SZU-1 increased, which may have weakened the overall strength of the rock. In contrast, the overall strength of the rock may have been strengthened due to thermal expansion, cold contraction, and fine-grained mineral precipitation and filling.

(2) When the vacuum level was less than 100 Pa, the thermal conductivity tends to be gentle with the decrease of vacuum level, indicating that air conduction could be almost ignored. When the vacuum level was greater than 100 Pa, the thermal conductivity increased significantly with increasing vacuum level, indicating that air conduction played the leading role.

(3) Within the test range, with increasing temperature, the specific heat capacity, thermal conductivity, and thermal expansion coefficient of SZU-1 showed a nonlinear increasing trend, while the thermal diffusivity showed a nonlinear decreasing trend. An exponential function could effectively
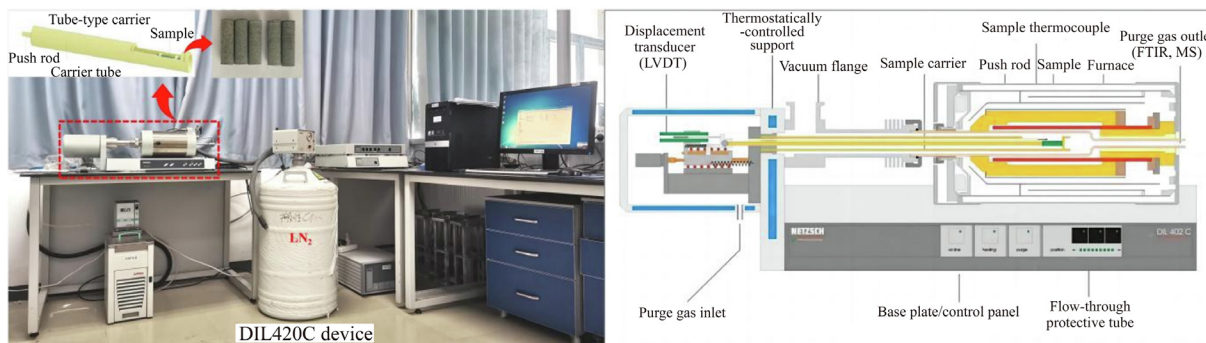

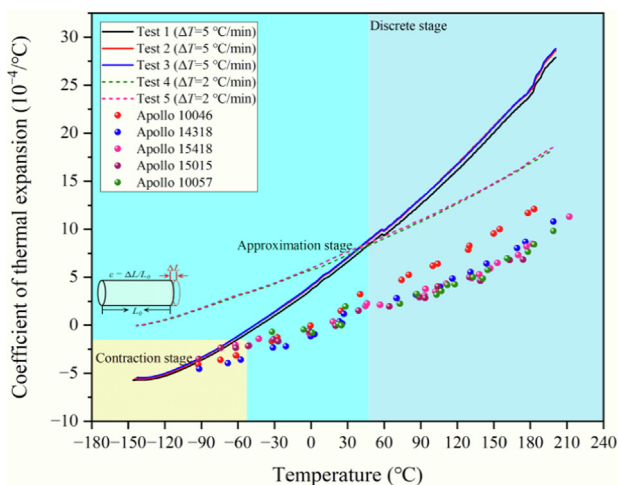**Fig. 16.** DIL420C device and the schematic diagram.

Fig. 17. Test data of SZU-1 thermal expansion coefficient in lunar-based extreme environment.

characterize the relationship between thermal conductivity, thermal diffusivity, and temperature.

Acknowledgments

References

[1] Ouyang ZY. Introduction to Lunar Science. Beijing: China Astronautic Publishing House; 2005.
[2] Xie HP, Zhang GQ, Luo T, Gao MZ, Li CB, Liu T. Scheme and design of a lunar large-depth and in-situ condition-holding coring robot system. Adv Eng Sci 2020;52(2):1–9. in Chinese.
[3] Xie HP, Zhang GQ, Li CB. Scheme of underground space utilization of lunar thermostatic layer. Adv Eng Sci 2020;52(1):1–8. in Chinese.
[4] Xie HP, Li CB, Sun LC, Liao JX, Yang W, Ma JC, Li BX. Conceptualization of in-situ energy support technology on the moon. Adv Eng Sci 2020;52(3):1–9. in Chinese.
[5] Liu XQ, Sun HB, Sun SL. Analysis of defense strategies of near-Earth asteroids. J Deep Space Explor 2017;4(6):557–63.
[6] French BM, Heiken GH, Vaniman DT. Lunar Sourcebook: A User's Guide to the Moon. Cambridge: Cambridge University Press; 1991.
[7] Li RL, Zhou GQ, Yan K, Chen J, Chen DQ, Cai SY, Mo PQ. Preparation and characterization of a specialized lunar regolith simulant for use in lunar low gravity simulation. Int J Min Sci Technol 2022;32(1):1–15.
[8] Wang S. Analysis and optimization on cutting and crushing rock of carbide drill based on LS-DYNA. Doctoral dissertation. Beijing: China University of Geosciences; 2016.
[9] Quan QQ, Shi XM, Tang DW, Deng ZQ, Jiang SY. Extraction and recognition of drilling characteristics on interface between simulants of lunar soil and lunar rock. Robot 2015;37(3):351–60.
[10] Li P. Research on efficient drilling characteristic of lunar regolith coring bit with low acting force. Doctoral dissertation. Harbing: Harbin Institute of Technology; 2017.
[11] Li BB. The drillability research of simulated lunar rocks based on physics and mechanics properties. Master's dissertation. Beijing: China University of Geosciences; 2015.
[12] Wang HG. The researches on the mechanism of heat transfer in the pross of drilling under the condition of simulated lunar rock. Master's dissertation. Beijing: China University of Geosciences; 2015.
[13] Li LY. Stress analysis of single cutter cutting lunar rocks simulants. Master's dissertation. Beijing: China University of Geosciences; 2015.
[14] Cui JS. Research on mechanics-thermotics characteristic of drill-lunar regolith interaction and prediction of the temperature field. Doctoral Dissertation. Harbin: Harbin Institute of Technology; 2016.
[15] Francl J, Kingery WD. Thermal conductivity: IX, experimental investigation of effect of porosity on thermal conductivity. J Am Ceram Soc 1954;37(2):99–107.
[16] Bastin JA, Clegg PE, Fielder G. Infrared and thermal properties of lunar rock. Science 1970;167(3918):728–30.
[17] Robie RA, Hemingway BS, Wilson WH. Specific heats of lunar surface materials from 90 to 350 degrees kelvin. Science 1970;167(3918):749–50.
[18] Cremers C, Birkebak R, Dawson J. Thermal conductivity of fines from Apollo 11. In: Proceedings of Apollo 11 Lunar Science Conference. New York: Pergammon press; 1970. p. 2045–50.
[19] Bernett EC, Wood HL, Jaffe LD, Martens HE. Thermal properties of a simulated lunar material in air and in vacuum. AIAA Journal 1963;1(6):1402–7.
[20] Fountain JA, West EA. Thermal conductivity of particulate basalt as a function of density in simulated lunar and Martian environments. J Geophys Res 1970;75(20):4063–9.
[21] Fujii N, Osako M. Thermal diffusivity of lunar rocks under atmospheric and vacuum conditions. Earth Planet Sci Lett 1973;18(1):65–71.
[22] Horai KI, Simmons G, Kanamori H, Wones D. Thermal diffusivity and conductivity of lunar material. Science 1970;167(3918):730–1.
[23] Horai K-I, Winkler Jr J. Thermal diffusivity of lunar rock sample 12002, 85. In: Proceedings of Lunar Science Conference. Oxford: Pergamon Press; 1975. p. 3207–15.
[24] Baldridge WS, Miller F, Wang H, Simmons G. Thermal expansion of Apollo lunar samples and Fairfax diabase. In: Lunar and Planetary Science Conference Proceedings. Cambridge, Massachusetts: MIT Press; 1972. p. 2599–609.
[25] Thirumalai K, Demou SG. Effect of reduced pressure on thermal-expansion behavior of rocks and its significance to thermal fragmentation. J Appl Phys 1970;41(13):5147–51.
[26] Richter D, Simmons G. Thermal expansion behavior of igneous rocks. Int J Rock Mech Min Sci Geomech Abstr 1974;11(10):403–11.
[27] Griffin RE, Demou SG. Thermal expansion measurements of simulated lunar rocks. In: AIP Conference Proceedings. College Park, Maryland: American Institute of Physics; 1972. p. 302–11.
[28] Cooper HW, Simmons G. The effect of cracks on the thermal expansion of rocks. Earth Planet Sci Lett 1977;36(3):404–12.
[29] Xu JM, Liu QS, Peng WW, Chang XX. Experimental study on basic mechanical behaviors of rocks under low temperatures. Chin J Rock Mech Eng 2006;25(12):2502–8. in Chinese.
[30] Ouyang ZY. Lunar geology. Adv Earth Sci 1994;9(2):80–1.
[31] Cai W, Li SL, Lu Y, Wu YZ. Study on basalt mineral composition of mare serenitatis. Acta Astron Sin 2018;59(6):51.
[32] Hu S, He HC, Ji JL, Lin YT, Hui HJ, Anand M, Tartèse R, Yan YH, Hao JL, Li RY, Gu LX, Guo Q, He HY, Ouyang ZY. A dry lunar mantle reservoir for young mare basalts of Chang'e-5. Nature 2021;600(7887):49–53.
[33] Zhang XM, Zhang XY, Chen Y, Cai W, Lu Y, Wu YZ. Mineralogy of mare frigoris. Earth Sci Front 2018;25(1):314–24.
[34] Qiao L, Chen J, Xu LY, Wan S, Cao HJ, Li B, Ling ZC. Geology of the Chang'e-5 landing site: Constraints on the sources of samples returned from a young nearside mare. Icarus 2021;364:114480.
[35] Yao YG, Xiao CJ, Wang PS, Li CL, Zhou Q. Instrumental neutron activation analysis of Chang'e-5 lunar regolith samples. J Am Chem Soc 2022;144(12):5478–84.
[36] Li BB, Zhou Q, He LZ, Du YS. Lunar rock sampling and the investigation & analysis on the physical and mechanical properties. Explor Eng (Rock Soil Drill Tunnel) 2015;42(5):1–7.
[37] Kiefer WS, Macke RJ, Britt DT, Irving AJ, Consolmagno GJ. The density and porosity of lunar rocks. Geophys Res Lett 2012;39(7):L07201.
[38] Cohn SN, Ahrens TJ. Dynamic tensile strength of lunar rock types. J Geophys Res - Solid Earth 1981;86(B3):1794–802.
[39] Che XC, Nemchin A, Liu DY, Long T, Wang C, Norman MD, Joy KH, Tartese R, Head J, Jolliff B, Snape JF, Neal CR, Whitehouse MJ, Crow C, Benedix G, Jourdan F, Yang ZQ, Yang C, Liu JH, Xie SW, Bao ZM, Fan RL, Li DP, Li ZS, Webb SG. Age and composition of young basalts on the Moon, measured from samples returned by Chang'e-5. Science 2021;374(6569):887–90.
[40] Huang JW, Li Z. X-ray Diffraction of Polycrystalline Materials: Experimental Principles, Methods and Applications. Beijing: Metallurgical Industry Press; 2012.
[41] Inistration SA. Study of mineral stability in the lunar environment. Washington, D.C.: National Aeronautics and Administration; 1968.
[42] Song M, Zhong YF, Ding CY, Liu YZ, Huang SP, Li QQ. Regolith mineral detection and abundance estimation based on the LMS spectral data of Chang'e-5 lander. Sci Sin Phys Mech Astron 2023;53(3):239607.
[43] Gu LX, Li JH. The focused ion beam (FIB) technology and its applications for earth and planetary sciences. Bull Miner Petrol Geochem 2020;39(6):1119–40. in Chinese.
[44] Lu GM, Feng XT, Li YH, Li SP, Su XX. Effect of microwave-induced fracturing of Chifeng basalt by a multi-mode cavity. Chin J Geotech 2020;42(6):1115–24. in Chinese.
[45] Gao MZ, Xie J, Yang BG, Tang RF, Deng HC, Liu YT, Ye SQ, Zhou XM, Wang SL. Characteristics and mechanism of rock 3D volume fracturing in microwave field. J China Coal Soc 2022;47(3):1122–37. in Chinese.

[46] Wu XH. Study on physical and mechanical properties and damage mechanism of granite at different heating temperatures after water-cooling. Doctoral dissertation. Beijing: University of Science and Technology; 2022.

[47] Fang SZ. Experimental study on the dynamic mechanical properties of weakly cemented red sandstone under sub-zero temperature. Doctoral dissertation. Beijing: China University of Mining and Technology; 2020. in Chinese.

[48] Yu W, Li XY, Wang SJ. Laboratory the thermal conductivity measurement of pyroxene powder under low temperature and atmospheric pressure conditions: Implication for the studies on lunar and Martian surface thermal environment. Acta Petrologica Sinica 2016;32(1):99–106. in Chinese.

[49] Li RL, Chen DQ, Zhou GQ, Li T, Mo PQ, Cai SY, Chen J, Ji YK. Development of terrestrial modelling system for lunar low gravity and vacuum environments. J China Univ Min Technol 2022;51(5):823–38. in Chinese.

[50] Chen C, Zhu CQ, Tang BN, Chen TG. Progress in the study of the influencing factors of rock thermal conductivity. Progr Geophys 2020;35(6):2047–57. in Chinese.